An Absolute Calibration of the Bay 4 Telescope Using Remote Laser Shots on October 20, 2001

Bruce Dawson[1], Brian Fick[2], John Matthews[3], Mike Roberts[3] and Paul Sommers[2]
1. Physics Department, University of Adelaide, Adelaide SA, Australia
2. University of Utah High Energy Astrophysics Institute, Salt Lake City Utah, USA
3. New Mexico Center for Particle Physics, University of New Mexico, Albuquerque, NM, USA
GAP-2002-10, March 2002

Abstract

We use remote laser shots to provide an end-to-end absolute calibration of the first Auger telescope at Los Leones. The aim is provide a cross-check for the preferred method using the local shell calibrator. We describe the laser method, including its challenges and limitations. We arrive at a calibration for the average response of mirror 4 of 1 ADC count = 5.1 photons of 355 nm wavelength arriving at the diaphragm.

1 Introduction

The proposed method for absolute calibration of the FD telescopes is an end-to-end procedure involving a cylindrical shell attached to the outside of the diaphragm. The entire diaphragm is illuminated with near uniformity by a light source calibrated in an absolute sense.

As a cross-check, we have undertaken a calibration with a remote laser, shot vertically into the atmosphere at a distance of almost 3 km from Los Leones. With a known laser intensity, and application of Rayleigh and aerosol scattering, we can predict the number of 355nm photons reaching the camera of the bay 4 telescope as a function of time. Comparing with the recorded profile, we get a calibration of ADC counts in terms of 355nm photons.

The laser was fired on the night of October 20, 2001 from a position at the centre of the field of view of bay 4 at a distance of 2.954 km at a position of (easting,northing) = (0459947, 6074728), with Los Leones at a position of (0459208, 6071872). Two sets of 50 shots were fired from the same position (run 87 and run 88). Both sets were nominally vertical, but the beam was rotated by 90° about the vertical axis between sets. This rotation was done to check the polarization state of the laser (see later). An energy probe at the laser monitored the intensity. The probe reading was averaged over ten shots, giving 5 readings per set of 50 shots.

The night of October 20 was clear with the aerosol horizontal attenuation length estimated to be in excess of 40 km. Bay 4 was fitted with the 2.2 m diameter diaphragm with a corrector ring. There was no borofloat glass window in the telescope diaphragm.

In addition to the distant laser shots, we have also fired lasers into the atmosphere directly outside the back door of the Los Leones building. These laser shots provide a near-uniform illumination of the telescope aperture allowing us to measure variations in pixel response across the camera.

2 Flat fielding with multiple-scattered laser light

A set of relative calibration constants has been derived using vertical laser shots just behind Los Leones made on October 18, 2001. The light from those shots got into all the pixels by scattering from the beam and then at least one other time. This multiple-scattered light provides a fairly uniform diffuse light intensity. There is no azimuthal variation and only modest dependence on elevation angle. We determine the elevation angle dependence empirically using the full

collection of pixels. The shell calibration system avoids this elevation angle dependence and should therefore be superior.

The flat-fielding for bay #4 reported here is based on data from cal_m04_000060.root_laser. The laser was positioned only 2 meters south of the Los Leones building door, and it was fired vertically at full power.

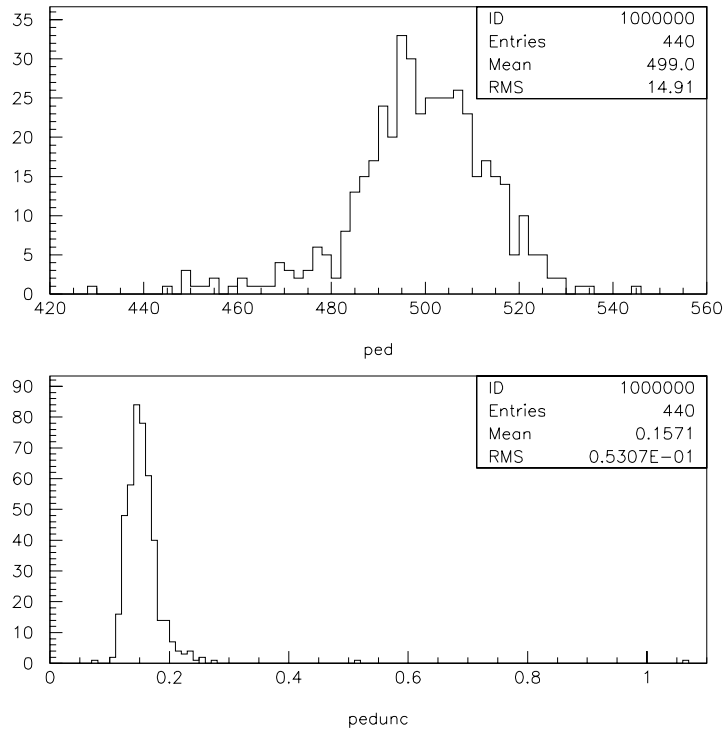

Figure 1: Distribution of pedestal values and pedestal uncertainties.

The traces for the events in this file are regrettably short, starting 250 time slices into the 100 microsecond buffers. The pulses start just before time slice 275. A pedestal is computed for each pixel and each event by averaging only 20 time slices 251-270. Better statistics are available, however, because of the 97 different laser shots. We can use the pedestal obtained by averaging the 97 pedestal determinations. Figure 1 shows the distribution of the 440 pedestals determined this way. The average pixel pedestal is 499 and there is an RMS spread of 14.9. The lower part of the figure shows the distribution of pedestal uncertainties, taken here to be the uncertainty in the mean of the 97 values that are used. The mean uncertainty is only 0.15 ADC count, which gives only a small signal uncertainty, even when the signal is a sum of 30 time slices.

The signal for each pixel and each laser pulse is taken to be the sum of ADC values in time slices 271-300 minus 30 times the pixel's mean pedestal. For each pixel, we then average the signal computed from the 97 different laser pulses. The uncertainty in the mean is computed by adding in quadrature the uncertainty in the mean ADC sum and the uncertainty in the subtracted mean pedestal sum.

Figure 2 shows how the signal depends on the camera row (elevation angle). The signals in each row have been averaged. The fitted line is $678+12\times row$. The lower part of the figure shows that the average residual is very small when this linear dependence is subtracted. Deviations from the linear fit have a 2.6% spread. This much uncertainty may be unavoidable with this

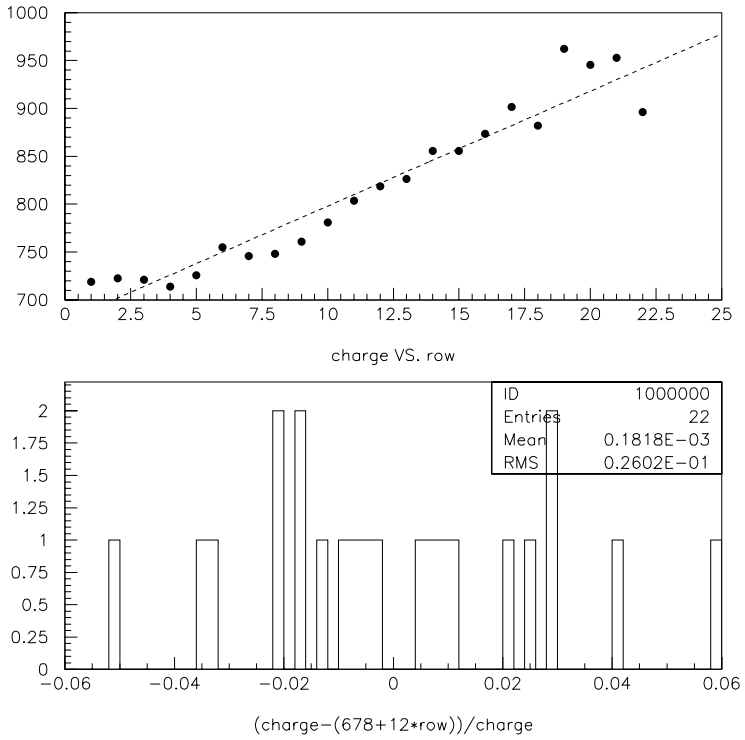

Figure 2: Elevation angle dependence of the signals. Each point in the upper plot is the average of a row. The lower plot shows the fractional residuals from the fitted linear dependence.

method.

It is assumed that each pixel receives a light flux that depends only on the row number according to the empirical linear relation. The flat-field calibration constant is then taken to be $(678 + 12 \times row)/signal$ for each pixel, where $signal$ is the signal for that pixel and row is its row number. Figure 3 shows the distribution of the resulting calibration scale factors. (There are 3 pixels that were poorly behaved and had large signal uncertainties. Their ID numbers are 13, 18, and 34. They are not included in the distributions of figure 3.) Note that the calibration constants have a spread of 13%. The lower part of the figure shows the distribution of statistical (fractional) uncertainties in the determination of the pixel signals. The mean is about 1%. (The more systematic 3% uncertainty from elevation angle dependence is not included.) If the signal uncertainties were not small compared to the calibration constant deviations from unity, then it would suggest that applying this calibration would be adding noise rather than reducing it. The fact that the 13% spread in calibration constants is large compared to the 1% statistical uncertainty in determining them indicates that this flat fielding does have merit.

3 Determining laser pulse intensities

A pickoff lens is used to direct a fraction of the laser intensity to a joulemeter. The measured energy is 10.1% of the light energy sent into the atmosphere. We are aware of a problem with running the laser at low power levels (necessary for these relatively nearby shots) where the frequency-doubled YAG output (green 532 nm light) is not as efficiently removed from the beam as it is at high power. The energy probe responds to this green light (as well as the

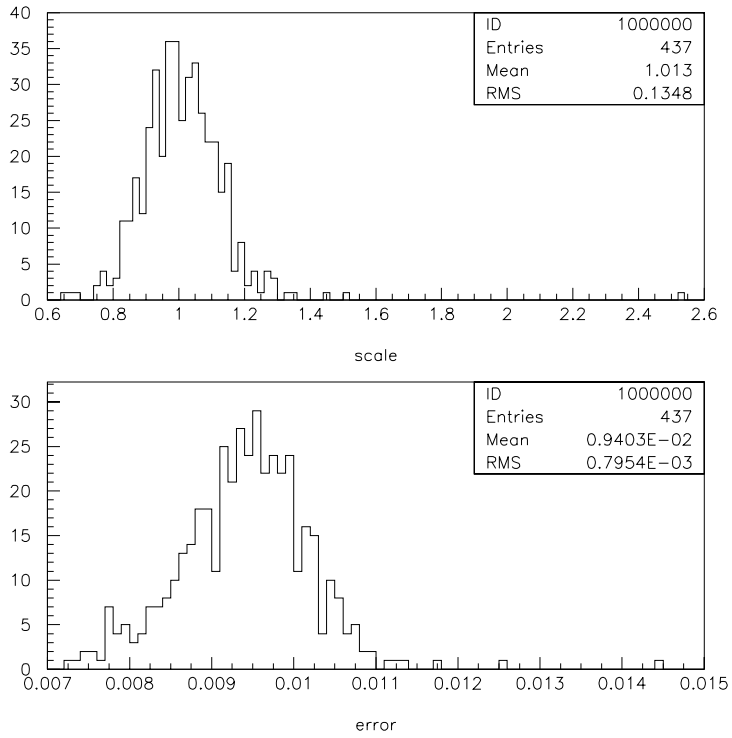

Figure 3: The distribution of calibration scale factors has a spread of about 13% (upper figure), whereas their mean statistical uncertainties are less than 1% (lower figure).

dominant 355 nm light) but the fluorescence detector does not. Thus an estimate of this green contamination was required.

The contamination has been measured in the lab at power level 10 to be less than 1% of the total energy. The shots on October 20 were at power level 2. Fortunately, some shots were also fired on that night at level 6 (an order of magnitude brighter than level 2) with the same geometry. Most pixels were saturated at level 6, but those that were not gave a ratio of UV brightness at the FD (level 6 to level 2) of 12.4. The joulemeter ratio between the shots was only 10.9. This implies that only 88% of the energy of the laser is at 355 nm at level 2. We use this factor to renormalize the laser energies before calculating the number of 355 nm photons emitted by the laser. Table 1 lists the laser intensities at ground level.

4 Laser polarization

The simulation employed in this study assumes a depolarized laser beam. For such a beam, the phase function for Rayleigh scattering has the familiar $1+\cos^2\theta$ dependence. However it seems that the laser used in the field on October 20 was still partially polarized, despite our attempts at depolarization. The evidence for this is demonstrated in Figure 4. Here we show the recorded light profiles for Group 4 of run 87 and Group 5 of run 88 (10 shots in each plot). These groups of shots had the same mean laser energy, but give very different light profiles at the detector, with run 88 profiles approximately twice as bright. This can be explained in terms of partial polarization of the laser pulse, and the resulting Rayleigh scattering. Rayleigh scattering is the principal means by which light is scattered towards the detector, especially on this night when the aerosol concentration was very low.

Our assertion is that our laser was partially polarized on the night, and that we can average the received light profiles from run 87 and run 88 to get the light profile expected from a totally depolarized beam. This is because of the 90° rotation of the laser about the vertical axis between the two runs.

Before discussing a partially polarized beam, consider a fully polarized one. Consider a polarized vertical laser with the electric vector oscillating in the direction towards the FD ("towards"). Now rotate the laser by 90° such that the electic vector is oscillating in a direction perpendicular to the FD direction ("perpendicular"). For the "towards" geometry the Rayleigh scattering phase function is $\cos^2\theta$ where θ is the angle between the propagation direction and

	Run 87		Run 88	
	joulemeter (μJ)	UV Photons	joulemeter (μJ)	UV Photons
Group 1	23.2	3.41×10^{14}	24.5	3.60×10^{14}
Group 2	22.6	3.32×10^{14}	20.5	3.01×10^{14}
Group 3	21.4	3.14×10^{14}	21.2	3.12×10^{14}
Group 4	21.7	3.19×10^{14}	16.9	2.48×10^{14}
Group 5	21.5	3.16×10^{14}	21.7	3.19×10^{14}

Table 1: For the two runs (laser vertical but rotated by 90° between runs) we list the laser probe energy and the number of UV photons emitted from the laser. We have applied a correction factor to the laser energy to account for some green light contamination. Each run has 5 groups of 10 shots over which the laser probe energy was averaged.

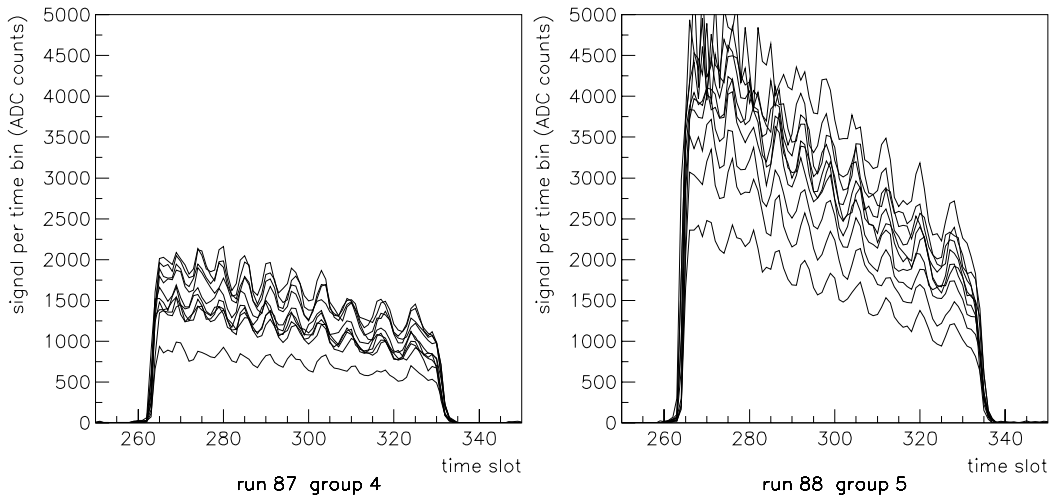

Figure 4: Two sets of 10 laser shots with the same mean laser energy, from group 4 of run 87 (left) and group 5 of run 88 (right). Time slots are 100 ns wide. All shots are vertical, but in run 88 the laser was rotated by 90° about the vertical axis. Within one plot, the different profile amplitudes are due to pulse-to-pulse variations in the laser output. However, the difference between the *mean* amplitudes in the left and right plots is due to the laser having a relatively strong polarized component. The bumps in the profiles are due to the variations in light collection efficiency across the camera.

the scattering direction. For the "perpendicular" geometry, the scattering is independent of θ and the phase function has a constant magnitude of 1 in these units.

A totally depolarized beam may be considered as a the average of these two polarized beams. This is the origin of the $1 + \cos^2\theta$ phase function for unpolarized light.

What about a partially depolarized beam? For that fraction of the beam that is unpolarized, the phase function will be $1 + \cos^2\theta$. The polarized part of the beam will have its plane of polarization in some arbitrary direction. We can represent this polarization with a linear combination of a "towards" (with amplitude "m" say) and a "perpendicular" (amplitude "n") polarized beam. Now rotate the beam by 90°. The amplitudes of two component beams will now switch, to "n" for the "towards" beam and "m" for the "perpendicular" beam. If we take the average of the original beam and the one rotated by 90°, the "towards" component has amplitude $\frac{m+n}{2}$ and the perpendicular component has amplitude $\frac{n+m}{2}$. In other words, the average of the two orientations has equal amplitudes in these polarization states, giving a $1 + \cos^2\theta$ scattering phase function. Note that this does not depend on the actual direction of the polarized component of the beam.

5 Analysis

The measured laser profiles (in ADC counts per 100 ns) are prepared by applying the flat-field corrections described above. These corrections average to unity over the entire camera, so this enables us to derive a single calibration constant for the camera.

We have employed the same simulation program used in an earlier study [1]. Briefly, we propagate a pulse of unpolarized 355 nm laser light into the atmosphere with some initial photon count. As the pulse propagates it is weakened by scattering, both Rayleigh and aerosol. Some of the scattering sends light in the direction of the detector. We propagate that light, and determine what fraction of it reaches the diaphragm of the bay 4 telescope. We thus simulate a light profile of 355 nm photons arriving at the diaphragm per 100 ns time slot.

Figure 5 shows some plots from the simulation, including the effect of changing the concentration of atmospheric aerosols. We assume a fixed scale height for the aerosols of 1.2 km, but we have set the ground level horizontal attenuation length to the following values: 10, 15, 20, 30, 50 km and ∞. As expected for these close-by laser shots, we find that there is little sensitivity to aerosols, particulary in the time domain between 280 and 325 time slots where we make our comparisons between data and simulation. We will use a 50 km attenuation length in all simulations that follow.

Here our analysis is complicated by the partially polarized laser beam, but we account for this by averaging results from runs 87 and 88.

Note that the recorded profiles in figure 4 are bumpy due to the variations in light collection efficiency across the camera. Light losses are minimized by the presence of the mercedes star collectors, but variations are still present. In the simulations shown in the first panel of figure 5 no such bumps are present, as we have stopped the simulation at the entrance to the telescope diaphragm, and just count photons entering the diaphragm. We will compare these smooth profiles with the bumpy recorded ones in order to extract a conversion factor between ADC counts and photons at the diaphragm. This is a true end-to-end calibration, and it means that we do not need to separately account for all the parameters of the telescope - filter transmission, mirror reflectivity, electronics gain, camera shadowing of the mirror etc. We have used close-by laser shots to flat-field the camera, effectively taking into account the variation in response across the camera surface. We are therefore justified in fitting a smooth simulated profile to the "average" of the bumpy recorded one.

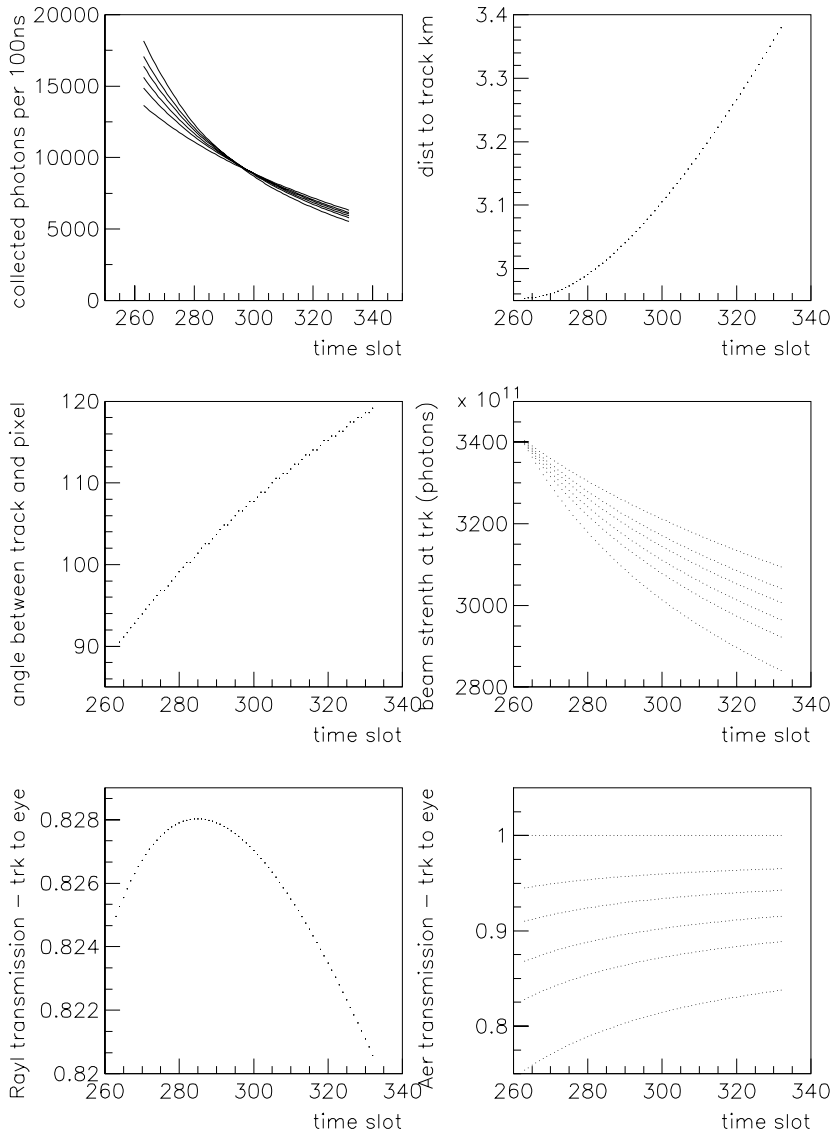

Figure 5: Some example plots from the simulation for run 87. The first plot shows the expected light signal at the diaphragm as a function of time for 6 values of the horizontal aerosol attenuation length (10, 15, 20, 30, 50 km and ∞) with the clearest atmosphere yielding the flattest profile. Other plots show how the distance to the laser track etc. change as a function of the time that light is received. Where more than one line is present in a plot, they refer to different aerosol concentrations.

However, it is interesting to see how a full simulation of the telescope compares with the recorded profiles. We show this comparison for illustration only. The simulation raytraces photons, therefore taking into account the effects of camera shadowing and the mercedes stars. We assume that 85% of photons hitting a mercedes will be reflected onto a pmt surface. Figure 6 shows the results from simulations overlaid with examples of recorded profiles. The agreement

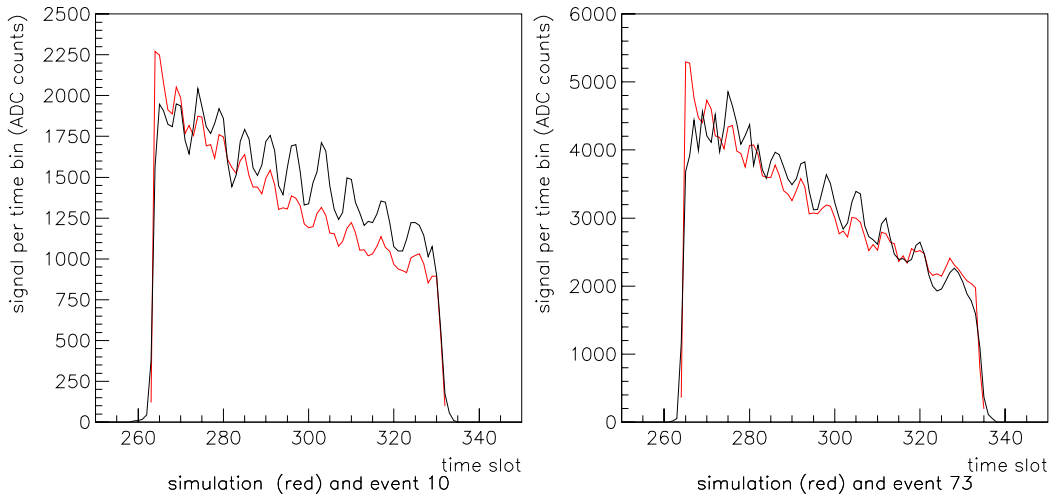

Figure 6: In red we show example simulations for group 1 of run 87 (left plot) and group 1 of run 88 (right). An aerosol attenuation length of 50 km is assumed. These are compared with one recorded profile from the particular groups (in black). Several features are evident. Simulations accurately match the overall widths of the profiles, and the positions and "phase" of the mercedes-induced dips in the light profiles. The amplitudes of the oscillations are not well simulated, partly because our raytracing code does not include the effect of the corrector ring. Note that the simulated profile is clearly steeper than the recorded one in run 87. (This is true for all profiles in run 87, not just the one displayed here). We believe this is related to the polarization state of the laser (see text).

is good in terms of the overall profile width, and the positions and "phase" of the bumps.

We find that it is necessary to tilt the assumed geometry in run 87 away from the vertical (by 1.1°) to match the width of the light profile and match the locations of the mercedes-produced dips. Detailed analysis of the pixel times using the known laser position confirms that the beam was tilted by about this much in run 87. For run 88, simulation of a vertical laser was sufficient to fit the width of the profile.

There is an obvious difference between simulations and data for one of the laser orientations. We find that the slope of the light profiles in run 88 is reasonably matched by simulations assuming a 50 km aerosol attenuation length. However, under this assumption the recorded light profiles from the other orientation, run 87, are consistently flatter than the simulations. This qualitative difference is consistent with expectations for a partiallly polarized beam, as demonstrated in the appendix.

Recall that simulations assume an unpolarized laser pulse. Part of the real laser pulse is polarized, and one can resolve that polarization electric vector (whatever its direction) into a "towards" and a "perpendicular" component. Consider early in the profile, when we are viewing the "towards" component of the polarized light almost end-on. Here we will not view any scattered light from that component, since the molecular dipoles excited by the "towards" vectors will not radiate in the direction of oscillation. However as the laser propagates upwards we will view these dipoles at a larger angle and we will start to see scattered light from that component of the polarized beam. The "perpendicular" component of the polarized part of the beam will

	Real Data ADC /100 ns	Unpolarized Simulation 355 nm Photons at Diaphragm/100 ns	Ratio
Group 1	1406	9670	6.878
Group 2	1332	9415	7.068
Group 3	1231	8905	7.234
Group 4	1292	9046	7.002
Group 5	1275	8961	7.028
Average			7.04 ± 0.13

Table 2: For run 87 we tabulate the mean ADC count and the simulated photon number per 100 ns. These numbers are calculated using data between time slices 270 and 320.

	Real Data ADC /100 ns	Unpolarized Simulation 355 nm Photons at Diaphragm/100 ns	Ratio
Group 1	2620	8400	3.206
Group 2	2344	7023	2.996
Group 3	2197	7280	3.314
Group 4	1923	5787	3.009
Group 5	2379	7444	3.129
Average			3.13 ± 0.13

Table 3: For run 88 we tabulate the mean ADC count and the simulated photon number per 100 ns. These numbers are calculated using data between time slices 296 and 324.

always be viewed at the same angle to the dipole, so its contribution to the light received (ignoring attenuation on its path to the eye) will not change. So it seems probable that in run 87 the electric vector of the polarized component of the laser is more "towards" than "perpendicular". This would produce a flatter profile than that expected for an unpolarized beam. A significant "towards" component is consistent with our understanding of the polarization direction of the YAG laser before the "depolarizing" optics. We believe that vector was pointing directly at Los Leones for run 87.

We continue with unpolarized simulations for the main results in this note. However, we have done simulations of a partially polarized beam to confirm the behaviour described in the previous paragraph. The results are described in the Appendix.

6 Results

Figures 7 and 8 show a comparison of recorded data and simulations for run 87 and run 88 respectively. For each group of 10 shots we have averaged the received light profile to make for a clearer comparison. We compare them with simulations of light arriving at the diaphragm.

The ADC to photons calibration is done in the following way. For each of the five "groups" of ten shots in the two runs we have a simulated profile, calculated using the mean laser energy for that group, and assuming an unpolarized beam. We then integrate the recorded and simulated profiles and compare. We choose a time range for the integration to avoid any signal saturation early in the profiles, and to reduce any dependence on aerosol assumptions. For run 87 we integrate between time slots 270 and 320 and we find the following mean ADC count per 100 ns for each of the five groups of shots: 1406, 1332, 1231, 1292 and 1275. These are listed in Table 2.

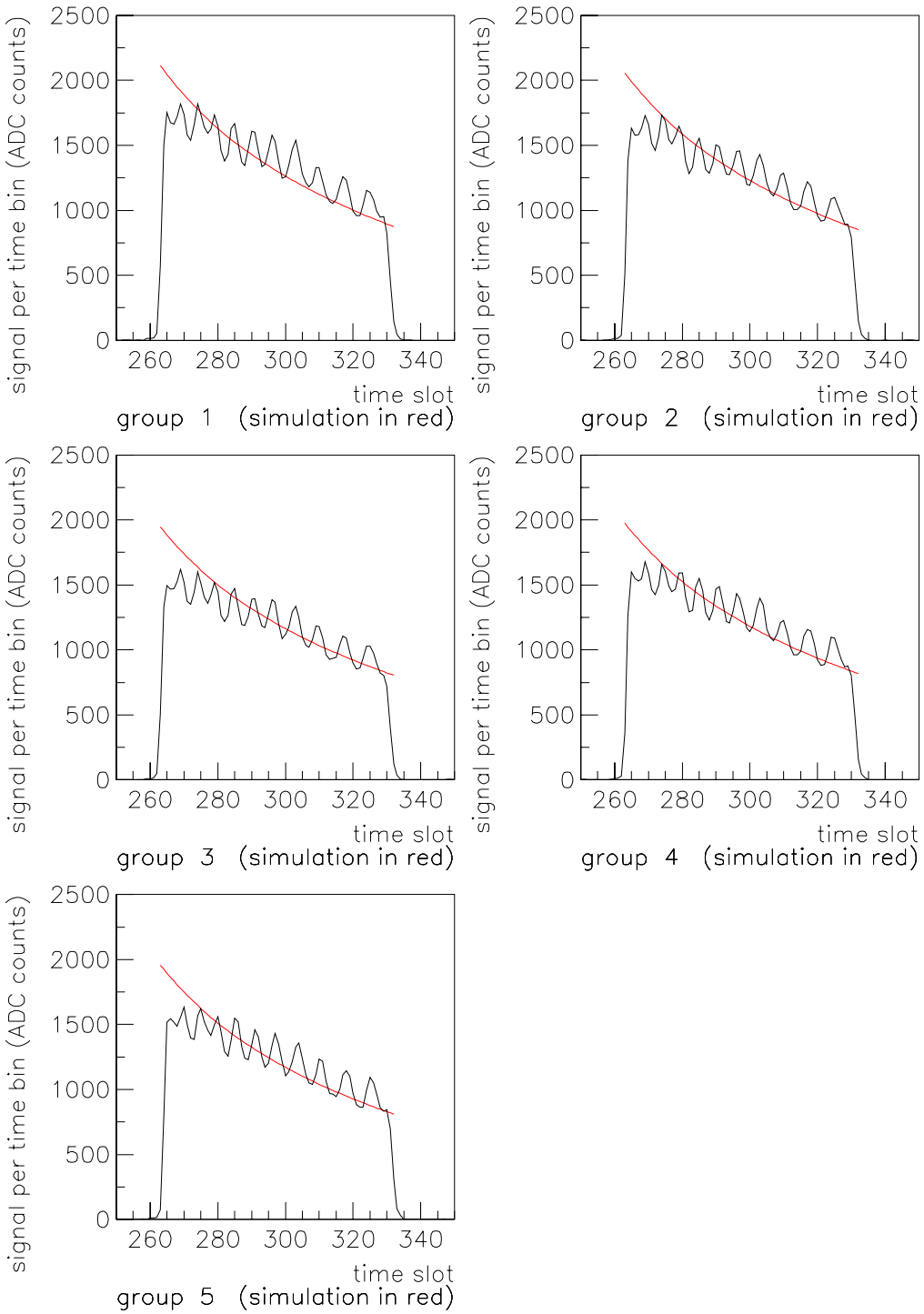

Figure 7: Data from the five groups of shots in run 87. We show the average recorded profile from the 10 shots, and compare it with the simulation (smooth line). The simulation predicts the photons arriving at the diaphragm entrance, and therefore does not show the mercedes bumps. The simulation assumes an aerosol attenuation length of 50 km and an unpolarized laser beam. The normalization has been determined by comparing the data and simulation in the time range between bins 270 and 320. See text.

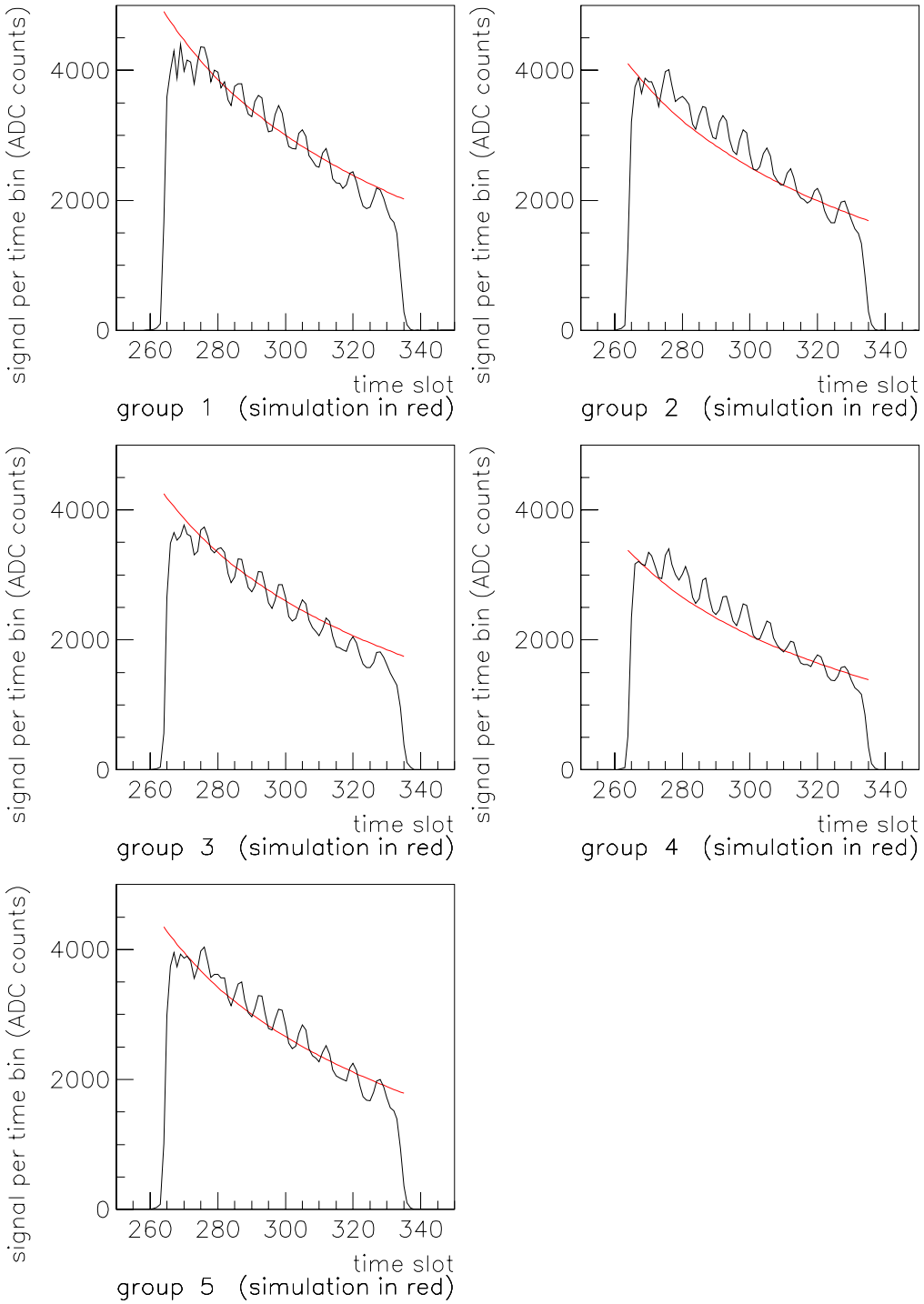

Figure 8: Data from the five groups of shots in run 88. Comments from the previous figure apply here, except that the normalization has been determined by comparing the data and simulation in the time range between bins 296 and 324 (narrower range than for run 87, but this avoids saturation in some profiles at earlier times).

There we also list simulation results in terms of the mean number of 355nm photons arriving at the diaphragm per 100 ns during the same time periods.

Table 3 shows the equivalent results for run 88, with the laser rotated by 90°. To get the true calibration constants we average the results of runs 87 and 88, since these averages are the appropriate numbers to compare with the unpolarized simulations. Thus, we arrive at the following calibration constant with statistical errors,

$$1 \text{ ADC count} = 5.09 \pm 0.09 \text{ photons (355 nm) at the diaphragm}$$

With some assumptions we can also derive a rough ADC to photoelectron calibration. We assume a 0.86 transmission factor for the optical filter at 355 nm, a 0.935 transmission factor for the corrector ring (the material has a transmission of 0.87, but only half the diaphragm is covered), a 0.90 factor for the reflectivity of the mirror, and 0.24 for the pmt quantum efficiency at 355 nm. It is also necessary to account for shadowing of the mirror by the camera, and the average light collection efficiency of the camera surface. From simulations, we estimate these two effects to amount to an efficiency of 0.724. Putting all this together we arrive at an estimate of 1 ADC count = 0.64 photoelectron. Clearly, many assumptions go into this number. That is why we prefer the "end-to-end" calibration given above which transforms ADC counts into photons arriving at the diaphragm.

7 Conclusion

We have used remote lasers to estimate the absolute calibration of the bay 4 telescope on October 20, 2001. We arrive at an end-to-end calibration of 5.1 photons (355 nm) per ADC count. The error in this number is dominated by systematics, not statistical uncertainties. Some of the systematic uncertainties will be eliminated or reduced in future measurements. In particular, the beam will be depolarized and the green light will be removed before the beam energy is measured. The joulemeter will be cross-calibrated for reliability. As seen in the first plot of figure 5, error in the aerosol model causes little error in the overall longitudinal normalization for a vertical laser beam at a distance of 3 km. Nevertheless, improved atmospheric monitoring in the future will improve the accuracy of the calculated light flux. When these systematic uncertainties are eliminated, this method of calibrating the FD telescopes via scattered laser light should provide an excellent end-to-end calibration.

The primary absolute calibration method will use the cylindrical shell ("dome calibrator") attached to the diaphragm. It will have even less systematic uncertainty and give an absolute end-to-end calibration of all pixels independently. The remote laser method described in this note provides a valuable cross-check of the shell calibration.

References

[1] B.R. Dawson, "June 2001 Laser Shots: Comparing Longitudinal Light Profiles with Expectations", Pierre Auger Project Technical Note GAP-2002-009 (2002).

A Appendix - Simulations with a Partially Polarized Beam

It is clear that the laser used for the measurements was not fully depolarized. We do not know the extent of the polarization, but we have taken account of the problem by averaging the results from run 87 and 88, given that there was a 90° rotation of the laser between runs.

We noted earlier that the unpolarized simulations do not exactly match the shape of the recorded profiles - for example in run 87 the simulations systematically gave profiles which were too steep. We decided to see if we could do better by introducing a polarized component to the simulated beam. Here we assume that the beam contains 50% of its energy in polarized light, and that the electric vector for this component is "towards" the detector in run 87. In essence this means that we take the Rayleigh scattering phase function to go as $0.5 + \cos^2\theta$ for run 87 and $1 + 0.5\cos^2\theta$ for run 88.

The results are shown in figures 9 and 10. Again we have normalized the simulations to the recorded profiles, over the time range 270-320 for run 87 and 296-324 for run 88. The agreement in shape is now better. In run 87 the simulations have flattened, and for run 88 they have steepened, as expected.

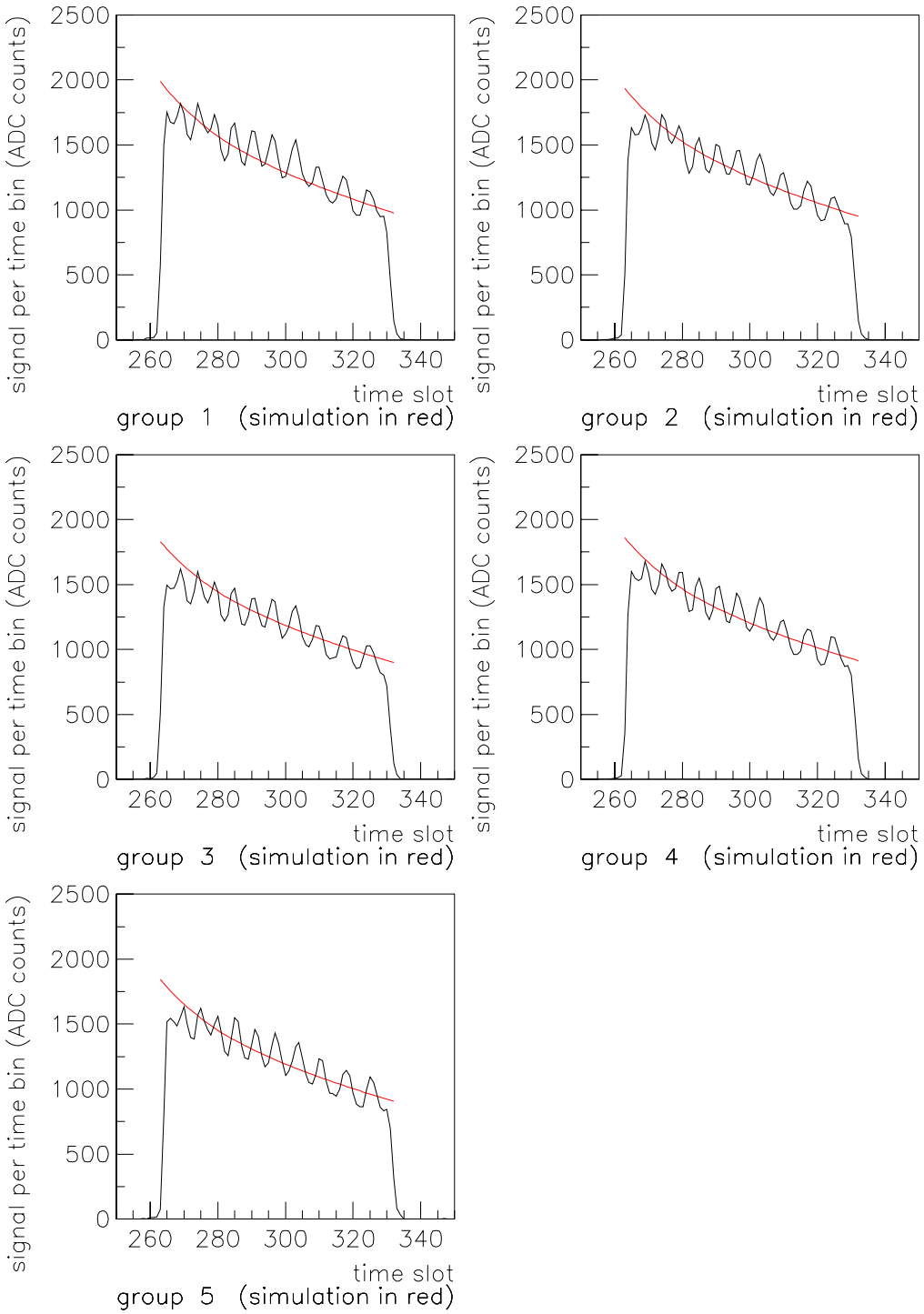

Figure 9: Data from run 87 (figure 7), but here we compare it with simulations for a one-half depolarized beam. The simulation is now about 20% flatter than for the totally depolarized beam, and is a better match in shape to the real data.

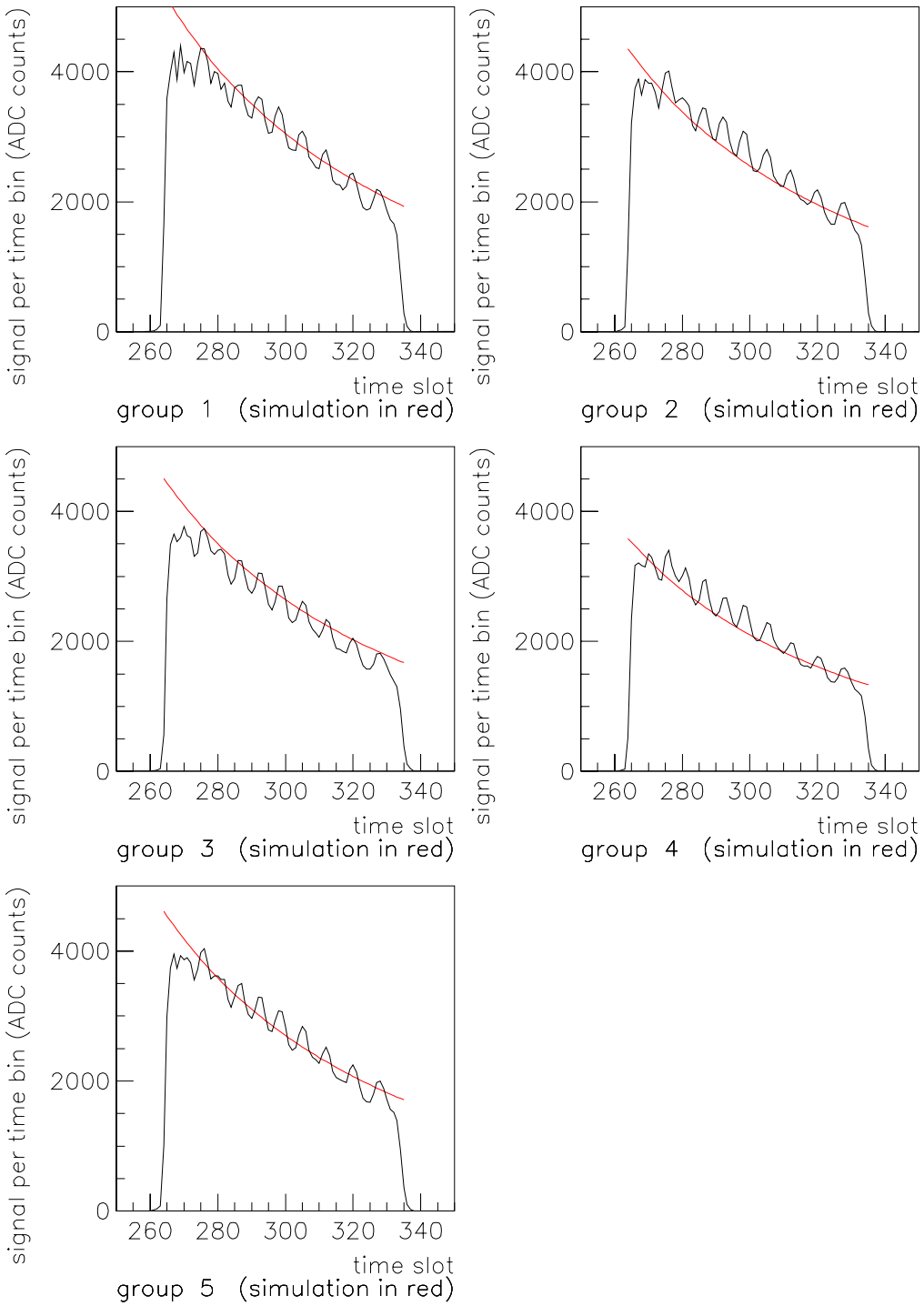

Figure 10: Data from run 88 (figure 8), but here we compare it with simulations for a one-half depolarized beam. The simulation is now about 10% steeper than for the totally depolarized beam, and is a better match in shape to the real data.